Impact of Ir modification on the durability of FeNC catalysts under start-up and shutdown cycle conditions

Carolin Prössl[a], Markus Kübler[a], Stephen Paul[a], Lingmei Ni[a,b], Simon-Johannes Kinkelin[c], Nils Heppe[a], Klaus Eberhardt[d], Christopher Geppert[d], Wolfram Jaegermann[b], Robert W. Stark[b], Michael Bron[c], Ulrike I. Kramm*[a,b]

Content:

Table S2. Summary of XPS results in wt% for Ir and Fe in all iridium modified catalysts together with the relative distribution of Ir^0 and Ir^{4+}. For reasons of comparison the results from NAA are added as well. The abbreviation n.d. indicated not determined, e.g. as no sample was left over, or for technical reasons.

Table S3. Summary of the ^{57}Fe Mössbauer parameters and assignment to iron signatures for the room temperature Mössbauer measurements.

Table S4. Model constraints and assignment for Fe 2p3/2 applied in this thesis and adapted from Serov et al., Biesinger et al. and Grosvenor et al.

Table S5. Model constrains and assignment for N1s signatures adapted from Artyshkova et al. and Jaouen et al..

Table S6. Model contrains and assignments of O1s peaks, adapted from Peukert et al. for Ir-O, Lindberg et al. for S-O/S=O and Smith et al for organics.

Table S7. Model contrains and assignments of C1s peaks, adapted from Polypenko et al and Smith et al.

Table S8. Model constrains and assignment for S2p species in this work, adapted from Lindberg et al.

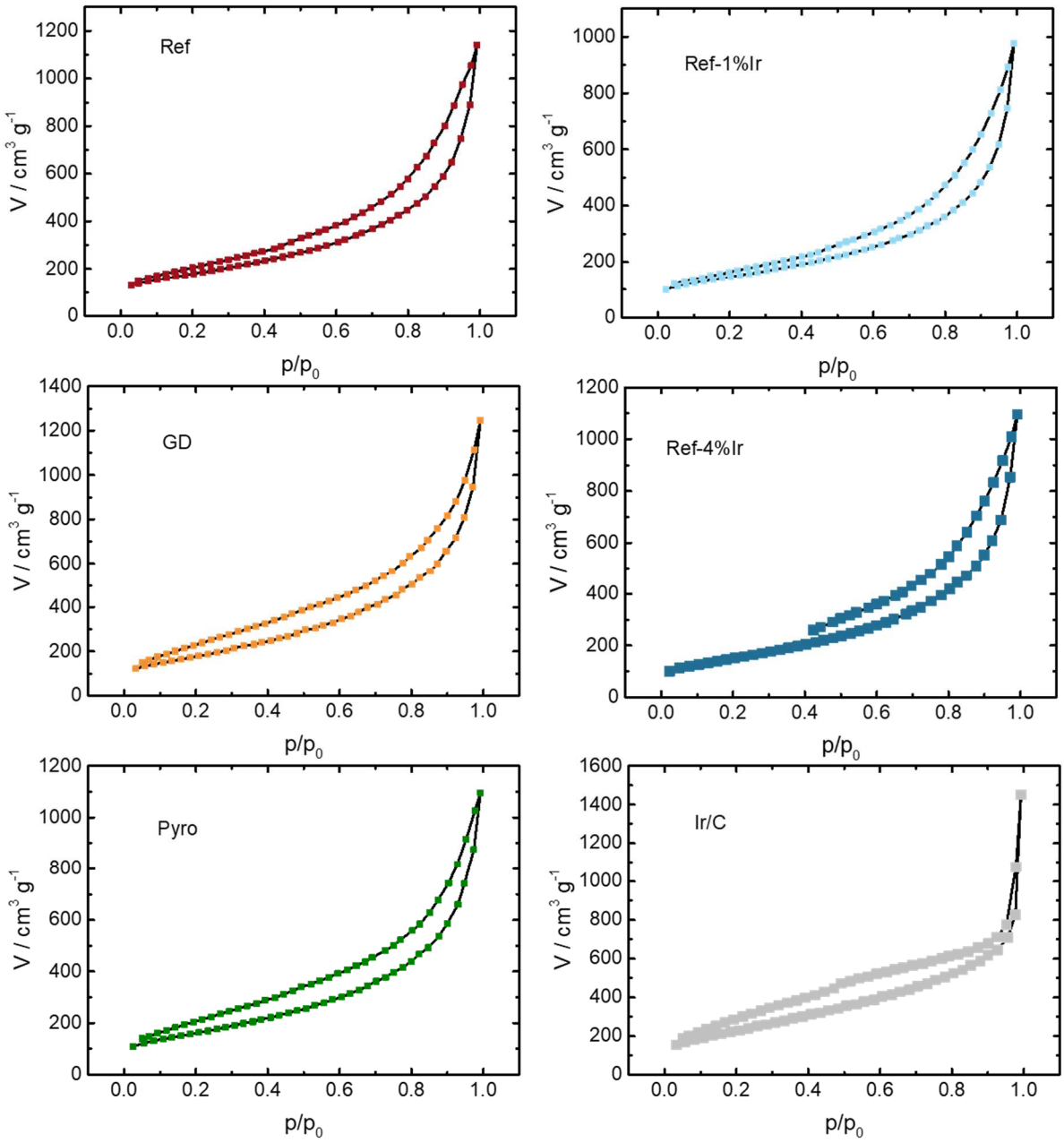

Figure S1. N_2 sorption measurements of the reference catalyst, Ir/C and the different Ir modified catalysts, as indicated.

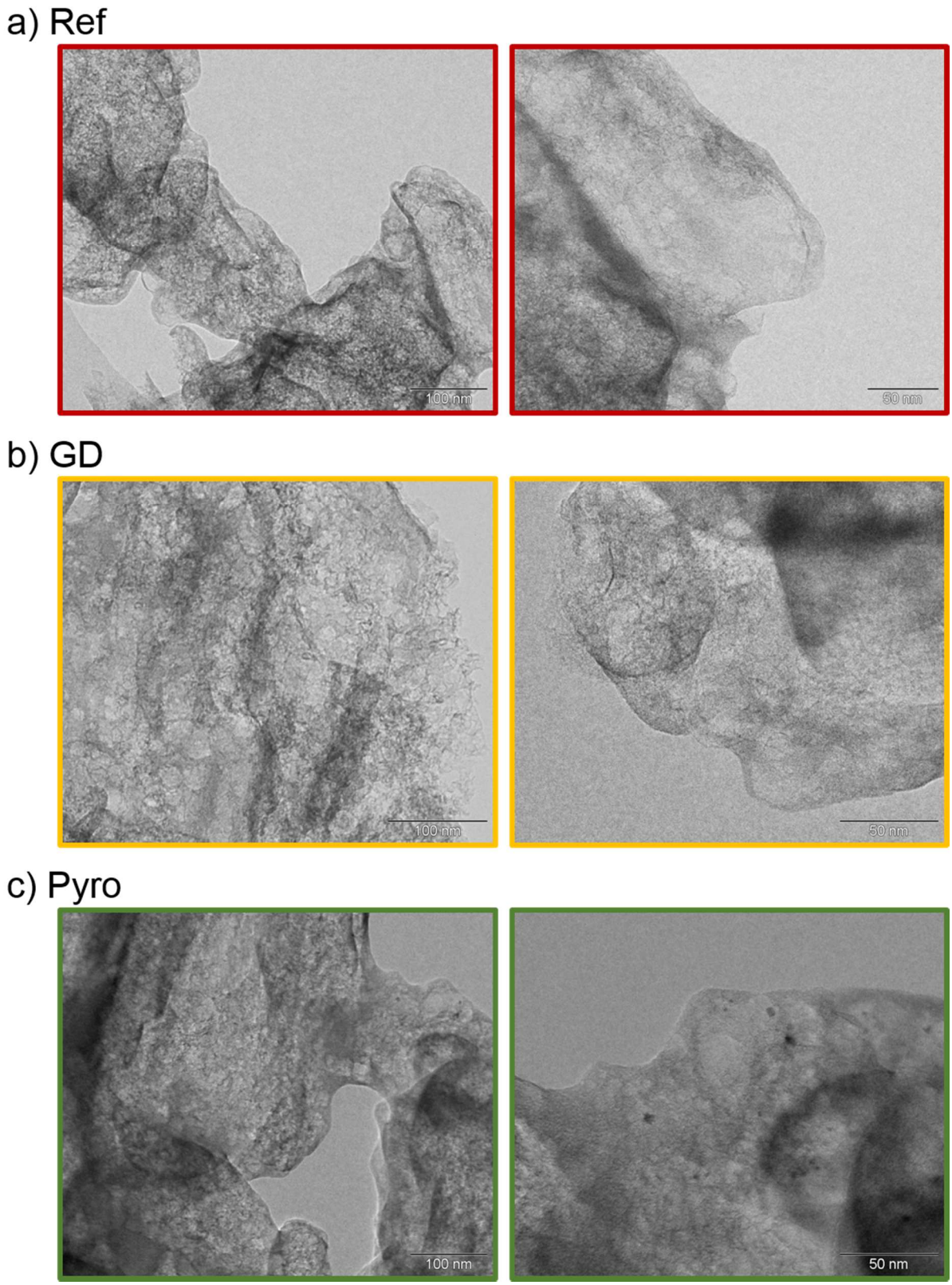

Figure S2: TEM images with 100 nm (left) and 50 nm scale (right) for the catalysts Ref, GD and Pyro, as indicated.

a) Ref-1%Ir

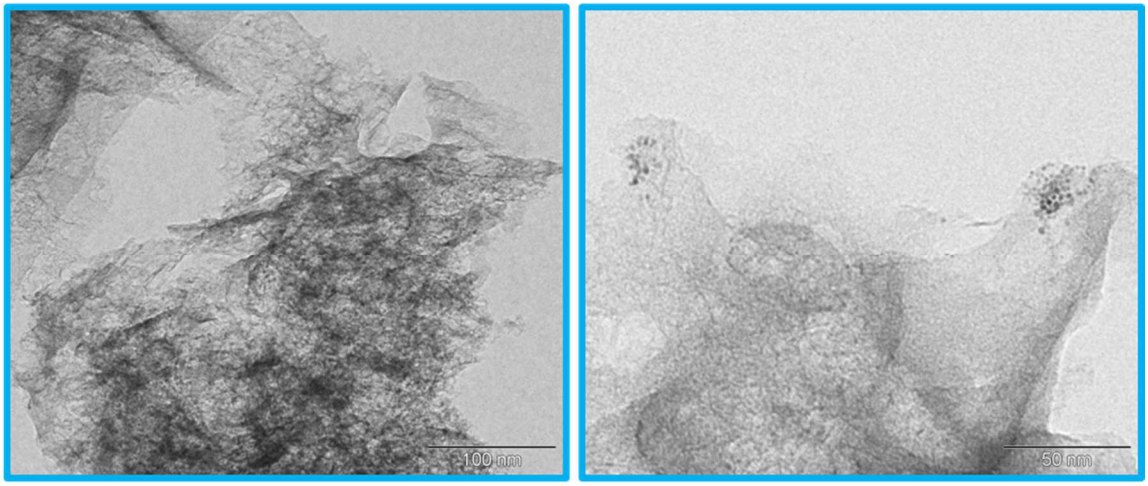

b) Ref-4%Ir

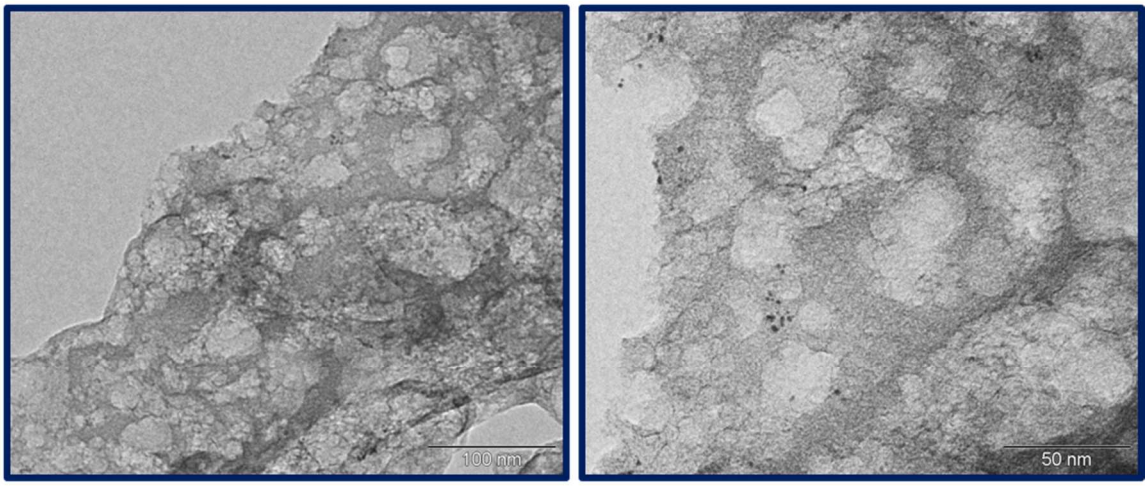

c) Ir/C – 1%

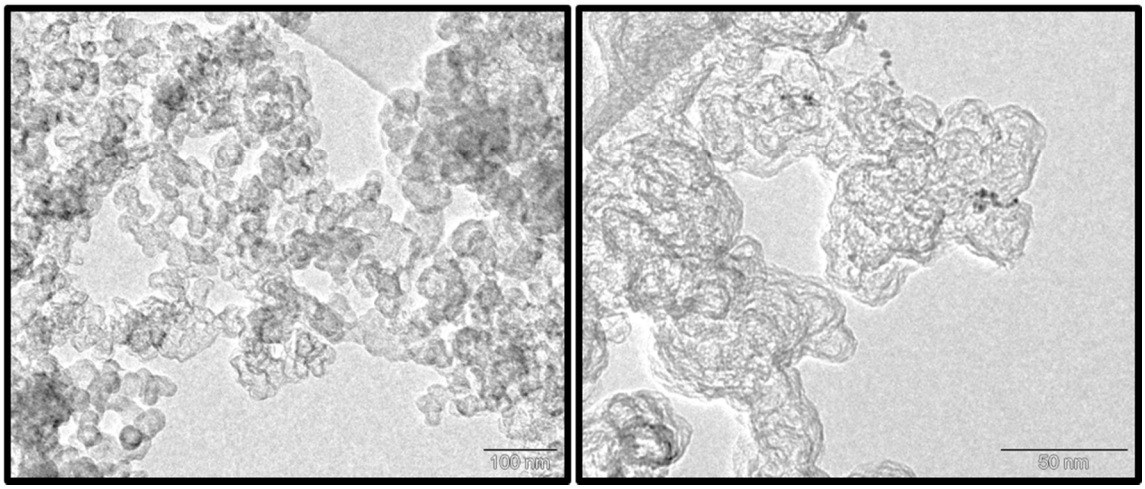

Figure S3: TEM images with 100 nm (left) and 50 nm scale (right) for the catalysts Ref-1%Ir, Ref-4%Ir and Ir/C – 1%, as indicated.

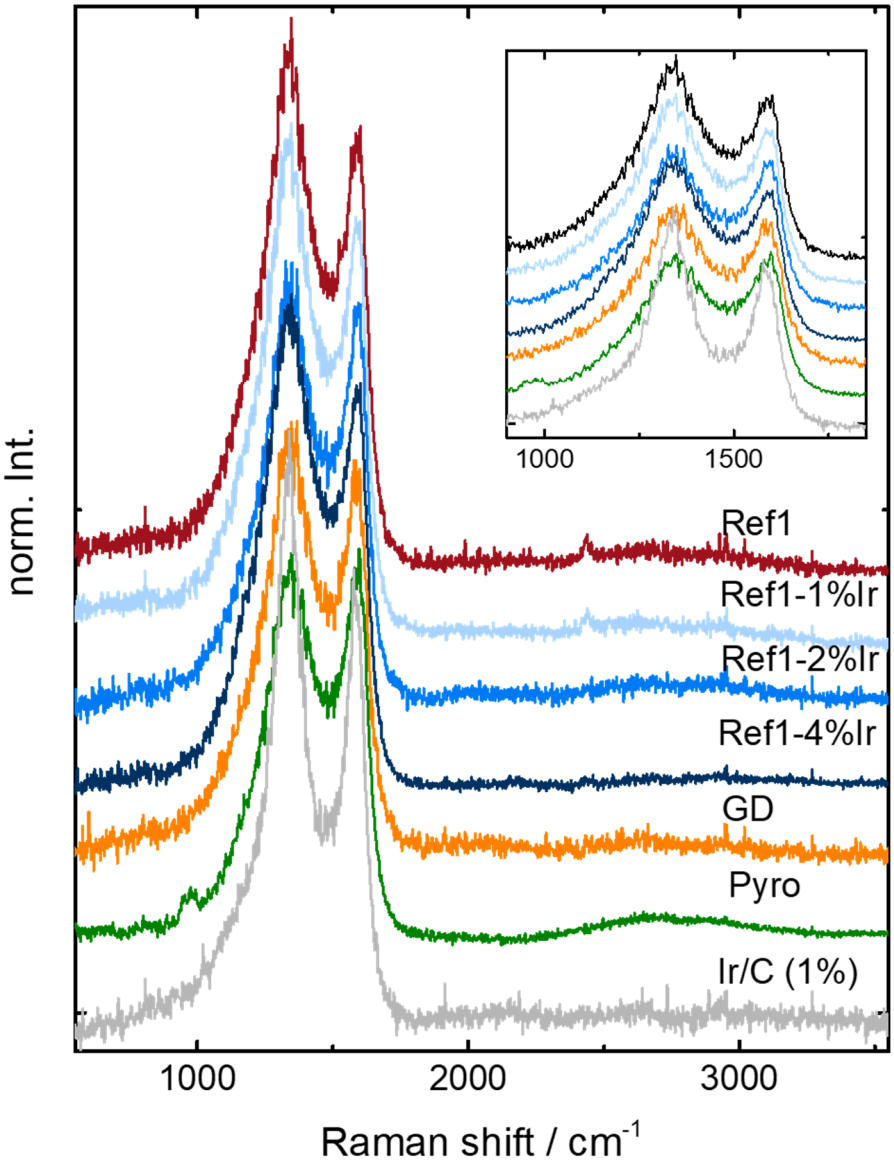

Figure S4. Raman spectra (averaged) of the different catalysts, as indicated. As insert the first order region of carbon between 900 – 1800 cm^{-1} is highlighted.

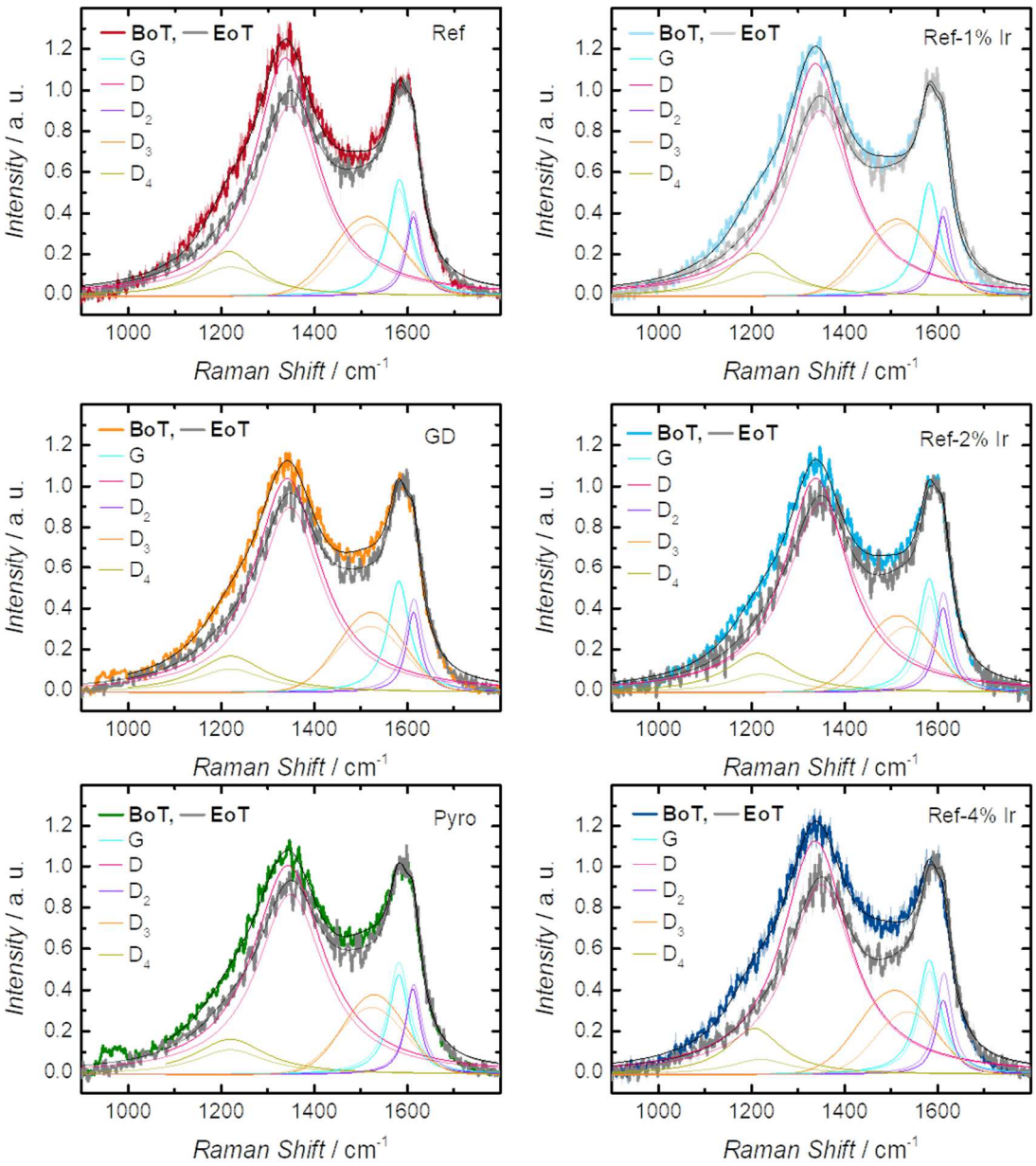

Figure S5. Comparison of the Raman spectra prior to SSCs (powder) and at EoT condition, together with the peak deconvolution. For peak deconvolution darker colors refer to the fitted bands in the initial catalyst and light colors are related to EoT condition.

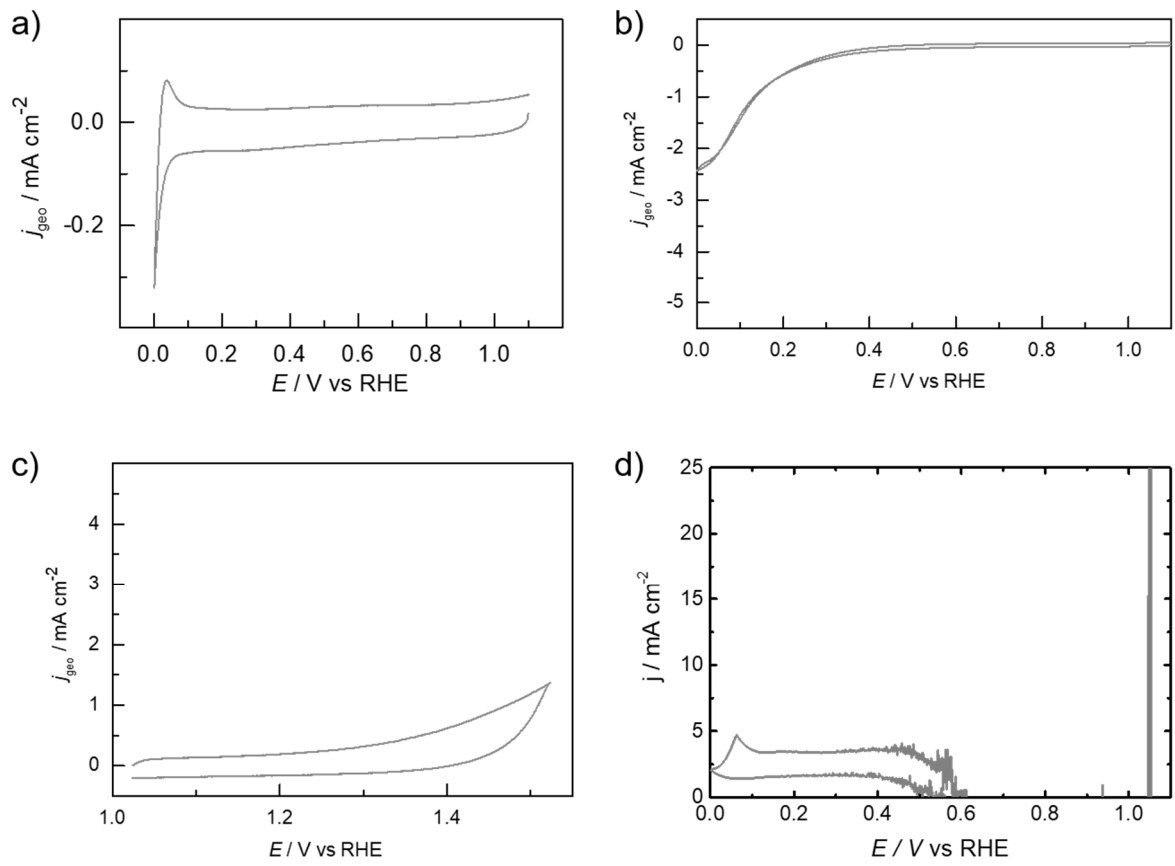

Figure S6. Cyclic voltammetry in (a), RDE at 1500 rpm (b), oxidative current in the high potential regime (c) and hydrogen peroxide formation (d) of the Ir/C catalyst. Measurements performed at a catalyst loading of 0.2 mg cm^{-2}, in a) and c) the 0.1M H_2SO_4 was saturated with nitrogen, while for b) and d) the electrolyte was saturated with oxygen. All measurements were made with a sweep rate of 10 mV s^{-1} .

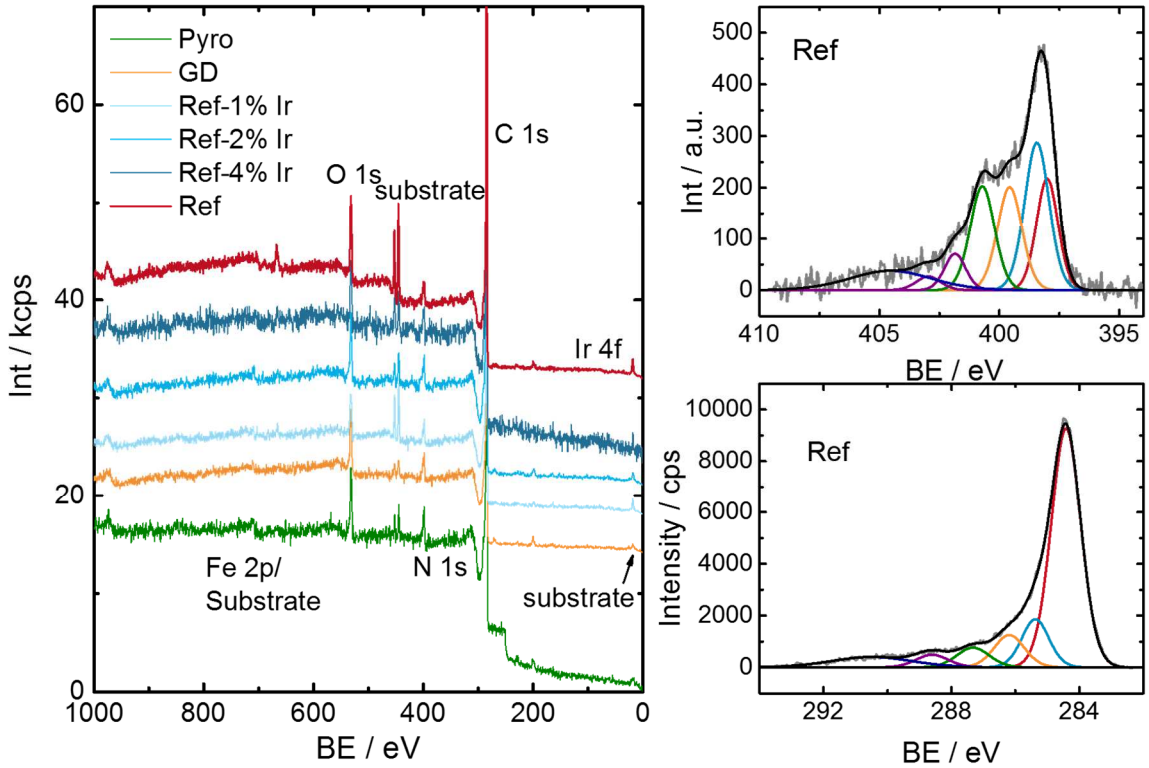

Figure S7. XP survey spectra of all Ir modified catalysts and Ref, indicated are the BE regions for Ir4f (62 – 68 eV), C1s (280 – 310 eV), N1s (395 – 410 eV), O1s (528 – 540 eV) and Fe2p (700 – 725 eV). All measurements performed on powdered samples pressed on In foil as substrate. Depending on the thickness of the catalyst layer, different amounts of In and In_2O_3 overlay the spectrum in the regions 695 – 705 eV, 435 – 465 eV and 15 – 20 eV. On the right side the N1s and C1s fine scan regions of Ref are shown, the color code for peak assignment is similar compared to the main manuscript.

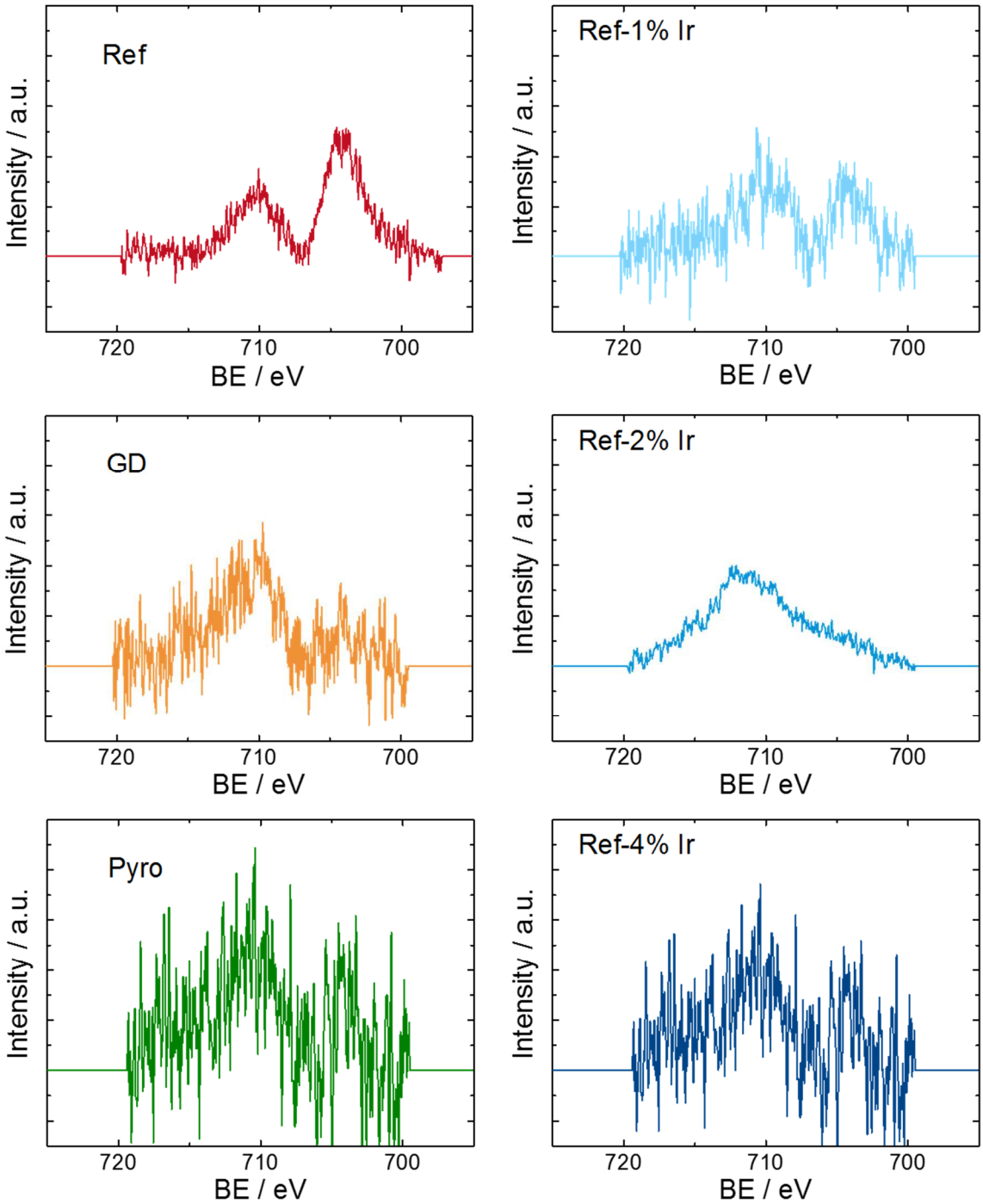

Figure S8. XP spectra of the Fe 2p region of Ref and all Ir modified FeNC samples. Note, to different extent the In substrate contributes in the energy range 695 – 705 eV.

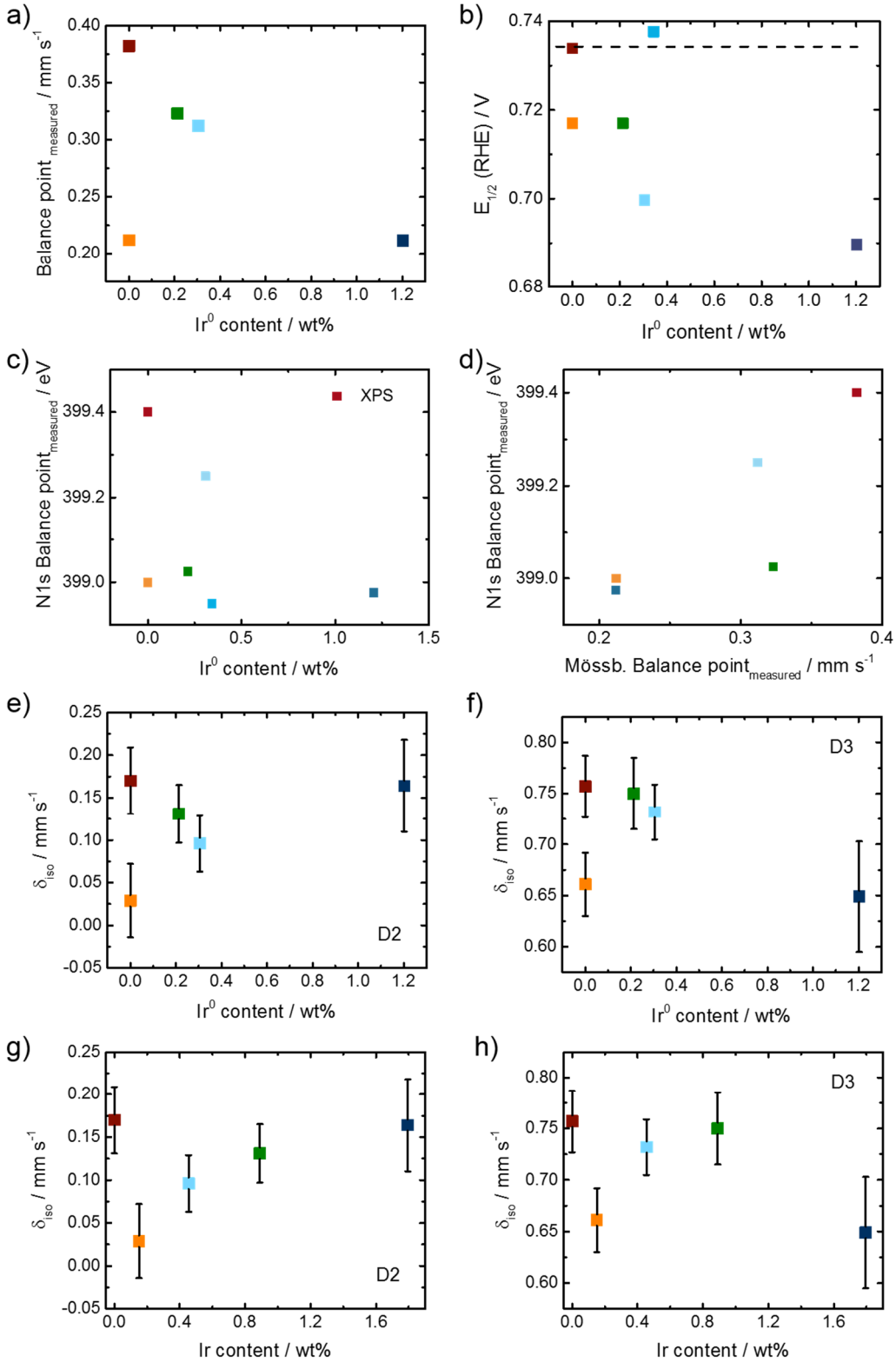

Figure S9. a) Balance points of the Mössbauer spectra, b) $E_{1/2}$ (BoT), c) Balance point of the N1s spectra and d) correlation between balance points of N1s spectra and Mössbauer spectra, e) isomer shift of D2 and f) isomer shift of D3, all as function of the Ir^0 content; in g) and h) the isomer shifts of D2 and D3 are given as a function of the overall Ir content. The catalyst Ref was prepared without Ir (Ir = 0), Ir values determined for all Ir modified samples by XPS.

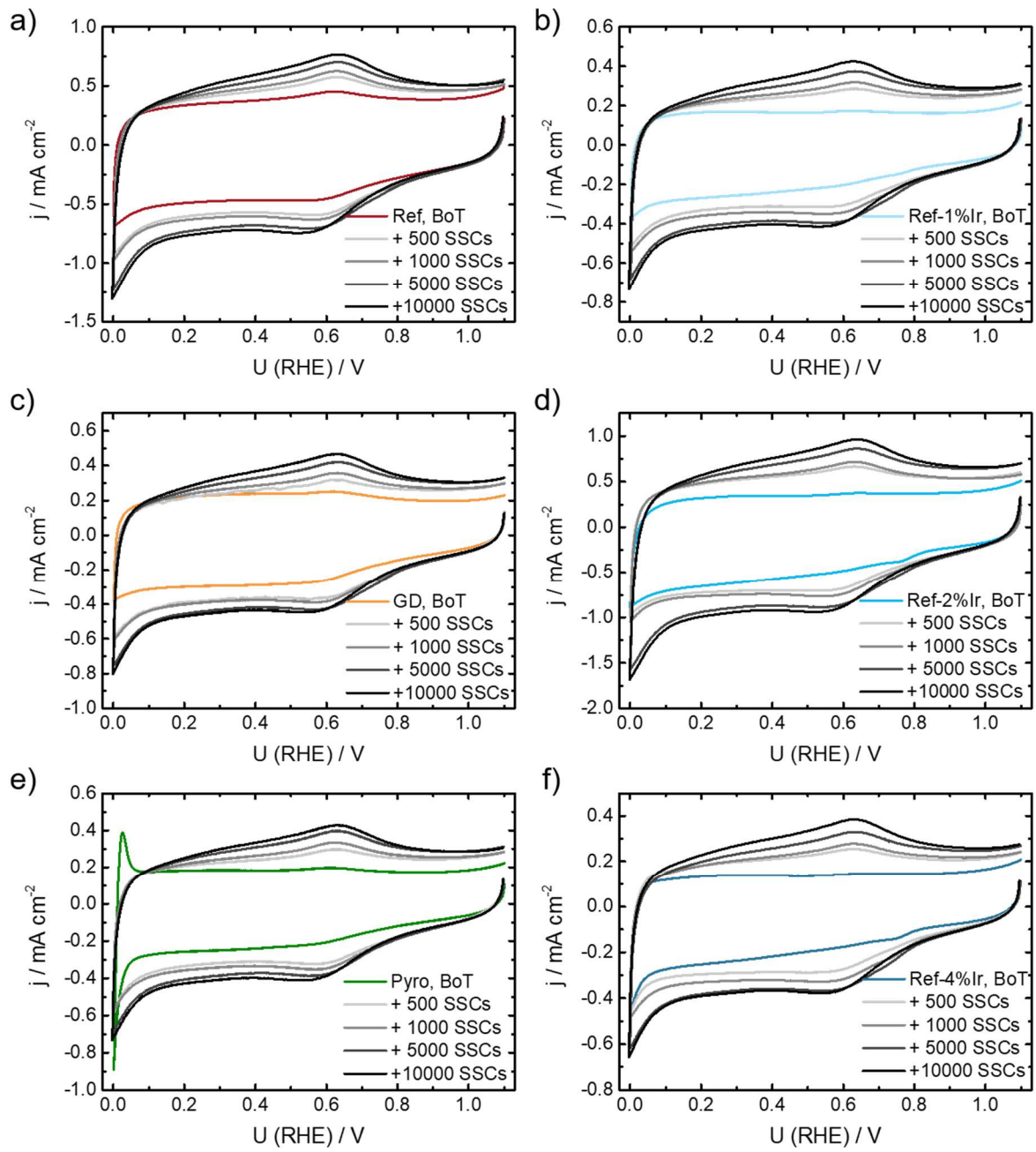

Figure S10. Evolution of the cyclic voltammograms in N_2 saturated of all samples over number of SSCs (BoT, 500, 1000, 5000 and EoT (10000)). All measurements performed with a sweep rate of 10 mV s^{-1}.

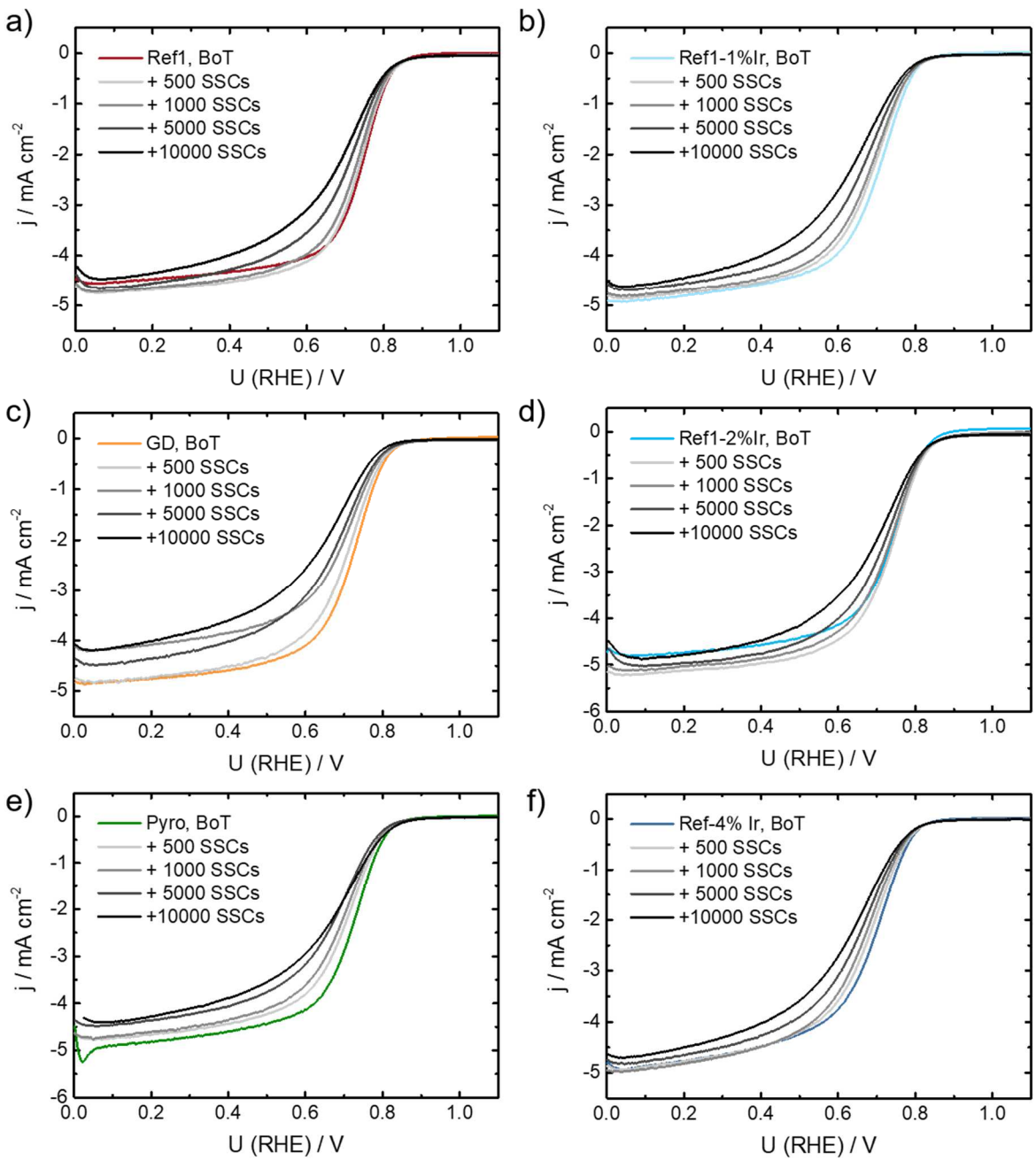

Figure S11. Evolution of the RDE measurements at rpm 1500 in O_2 saturated of all samples over number of SSCs (BoT, 500, 1000, 5000 and EoT (10000)). All measurements performed with a sweep rate of 10 mV s^{-1}.

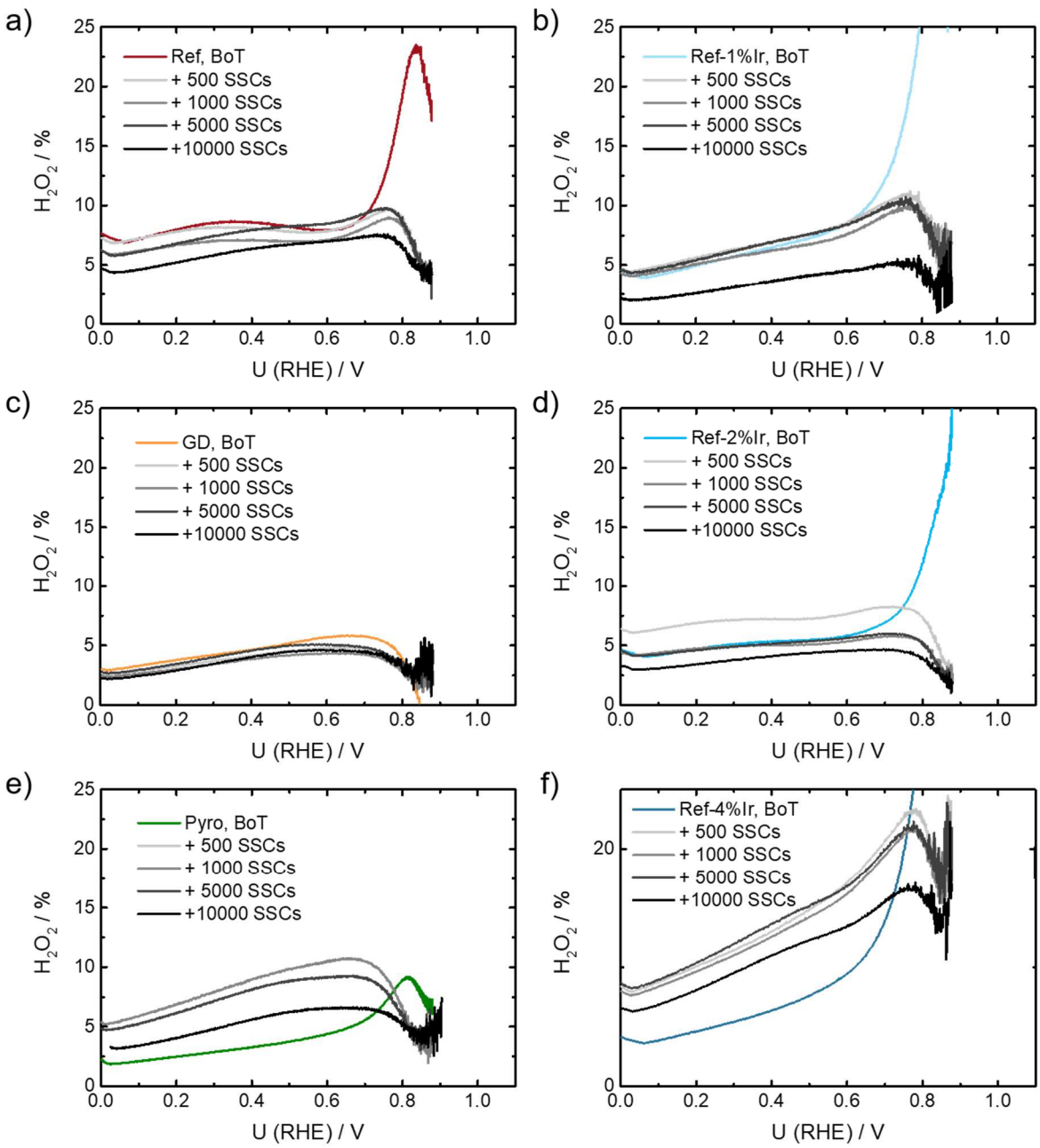

Figure S12. Change in H_2O_2 formation at rpm 1500 in O_2 saturated of all samples over number of SSCs (BoT, 500, 1000, 5000 and EoT (10000)). All measurements performed with a sweep rate of 10 mV s^{-1}.

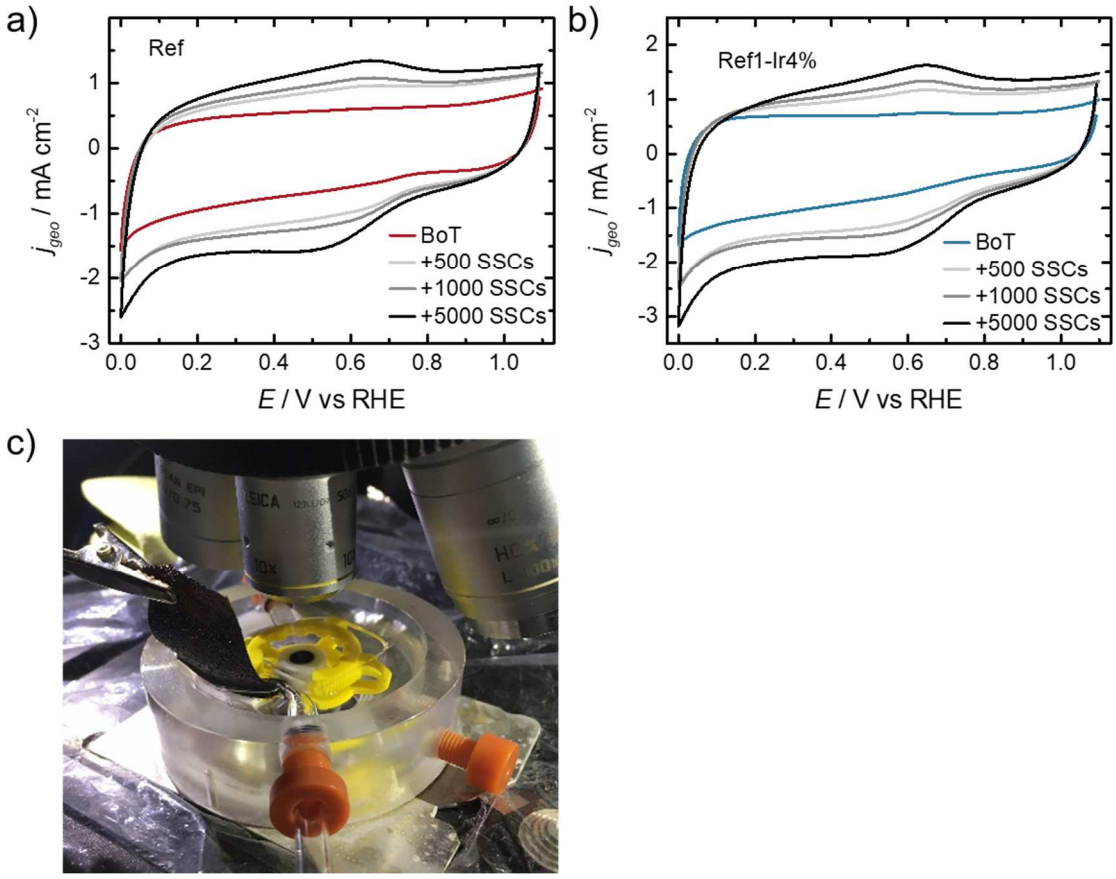

Figure S13. Cyclic voltammetry at 50 mV s^{-1} in the in-situ Raman setup at BoT and EoT (+5000 SSCs) for the Ref catalyst (a) and Ref-4% Ir (b). Measurements performed in Ar-saturated 0.1M H_2SO_4. c) Picture of the in-situ cell underneath the Raman microscope.

Table S1. Summary of EDS results of the catalysts Ref, GD, Pyro, Ref-1%Ir, Ref-4%Ir and Ir/C. Errors are indicated for the significant digit.

Catalyst	C /wt. %	N /wt. %	O /wt. %	S /wt. %	Cl /wt. %	Fe /wt. %	Ir /wt. %
Ref	92.7(4)	1.7(4)	2.5(1)	0.73(5)	0.93(4)	1.49(5)	n.d.
Ref-Ir1%	92.1(4)	2.2(4)	2.8(1)	0.60(5)	0.94(4)	1.36(5)	0.1(1)
Ref-Ir4%	92.3(3)	1.5(3)	2.55(9)	0.69(5)	0.98(4)	1.46(4)	0.6(1)
GD	92.3(3)	0.24(6)	3.29(7)	0.82(3)	1.40(3)	1.89(5)	0.02(3)
Pyr	91.13(3)	0.6(3)	4.4(3)	0.70(7)	1.19(9)	1.53(15)	0.6(2)
Ir/C	99.5(7)	n.d.	1.1(1)	0.11(6)	0.04(1)	0.15(10)	0.1(1)

Table S2. Summary of XPS results in wt% for Ir and Fe in all iridium modified catalysts together with the relative distribution of Ir^0 and Ir^{4+}. For reasons of comparison the results from NAA are added as well. The abbreviation n.d. indicated not determined, e.g. as no sample was left over, or for technical reasons.

	Ref	Ref-1% Ir	Ref-2% Ir	Ref-4% Ir	GD	Pyro
Ir / wt%	n.d.	0.46	0.60	1.80	0.15	0.89
Ir^0 area / %	n.d.	67	57	67	0	24
Ir^{4+} area / %	n.d.	33	43	33	100	76
Fe / wt%	1.19	1.10	1.36	1.35	1.10	1.60
Ir (NAA) / wt%	n.d.	n.d.	0.61	1.27	0.11	0.74
Fe (NAA) / wt%	2.59	n.d.	n.d.	n.d.	n.d.	n.d.

Table S3. Summary of the averaged ^{57}Fe Mössbauer parameters with standard deviation (SD) and assignment to iron signatures for the room temperature Mössbauer measurements. Averaging was made over the five individual measurements. Based on this, the SD includes the Ir-induced shift of some of the parameters. Errors in IS and Eq determination for the individual sites are indicated in Figure 6a.

	D1	SD	D2	SD	D3	SD
δ_{iso} / mm s^{-1}	0.35	0.02	0.12	0.06	0.71	0.05
ΔE_Q / mm s^{-1}	0.96	0.11	2.59	0.14	2.46	0.12
Assignm. / **Area / %**	**L-FeN_4-O_2** Ferrous low spin or ferric high spin, L representing an additional axial ligand [1, 2]		**Cl-FeN_4** Ferric intermediate spin [3]		**$(L)_{1-2}$-FeN_4** Ferrous high spin, 5- to 6-fold coord., L representing weak axial ligands [4]	
Ref	43.5	2.8	29.5	2.5	26.9	2.7
Ref-1%Ir	42.1	3.7	27.7	2.6	30.3	3
Ref-4%Ir	45.5	2.7	29.4	2.3	25.2	3.2
GD	42.1	3.7	27.7	2.6	30.3	3
Pyro	45.5	2.7	29.4	2.3	25.2	3.2

Table S4. Model constraints and assignment for Fe 2p3/2 applied in this thesis and adapted from Serov et al., Biesinger et al. and Grosvenor et al..[5-7]

Fe $2p_{3/2}$ Δ=13 eV	**Pre-Peak**	**Fe-N_x**	**Fe-Ox**	**Satellite**
Assignment	Pre-peak or Fe^0	N bonded Fe	3-4 Fe^{2+}/Fe^{3+} oxide peaks with Δ=1 eV	3-4 Satellite peaks of Fe^{2+}/Fe^{3+} oxides with Δ=1 eV
***BE* /eV**	707.5-705.8	708.0-708.9	709.0-714.0	714.0-716.0
***fwhm* /eV**	1.1-1.4	1.1-1.4	1.1-1.4	1.5-3.0

Table S5. Model constrains and assignment for N1s signatures adapted from K. Artyshkova et al. and F. Jaouen et al.[8, 9]

N 1s	**N≡C,**	**N_{Pyrid}**	**Me-N_x**	**N_{Pyrrol}**	**N_{graph}**	**N_{graph}**	**N_{ox}**
Assignment	Nitrile	Pyridinic	Metal coordinated	Pyrrolic	Graphitic N_1-position and quaternary N^{+4}	Graphitic N_2- and N_3-position	Oxidized
***BE* /eV**	397.7-398.1	398.4-398.8	399.2-399.9	400.6-400.9	401.6-402.3	402.9-403.2	402.0-405.2
***fwhm* /eV**	1.0-1.2	1.0-1.2	1.0-1.2	1.0-1.2	1.0-1.2	1.0-1.2	1.0-4.0

Table S6. Model contrains and assignments of O1s peaks, adapted from Peukert et al. for Ir-O, Lindberg et al. for S-O/S=O and Smith et al for organics.[10-12]

O 1s	**Me-O**	**OH**	**O-R**	**C=O, S=O**	**H2Oads**
Assignment	Metallic lattice oxides Ir-O, In-O	Hydroxyl species Me-OH, C-OH	Ether bound to carbon C-O, S-O	Carbonyl and carboxylic groups	Adsorbed water/oxygen, sub monolayer
BE /eV	529.5-530.2	530.9-532.0	532.1-532.9	533.0-534.0	534.8-535.2
fwhm /eV	1.0-1.2	1.0-1.2	1.5-2.2	1.5-2.2	1.0-3.0

Table S7. Model contrains and assignments of C1s peaks, adapted from Polypenko et al and Smith et al..[12, 13]

C 1s	**C=C, C-H sp2**	**C-H sp3**	**C-O, C-N**	**C=O, N-C-O**	**O-C=O, N-C=O**	**π-π* shakeup**
Assignment	Primary C-C/C-H peak with aromatic rings, aliphatic chains, graphitic C=C	Defects, step edges, clusters, sp3 bonded C, C-C(O)	Ether (C-O-C), hydroxyl C-OH bonded C, N bounded C of pyrrolic, pyridinic and graphitic	Carbonyl groups and carbons attached to two hydroxyl or ether groups	Carboxyl (C-OOH), ester (CO-C=O) groups, N-C=O	HOMO-LUMO transition of primary C-C peak
BE /eV	282.2-284.6	284.8-285.5	285.9-286.6	286.7-287.7	288.3-288.9	290.5-292
fwhm /eV	1.0-1.2	1.0-1.2	1.0-1.2	1.0-1.2	1.0-1.2	2.0-3.5

Table S8. Model constrains and assignment for S2p species in this work, adapted from Lindberg et al..[11]

S 2p Δ=1.2 eV	**MeSx**	**C-SH**	**C-S-C**	**C-S(O)-C**	**S-Ox**
Assignment	Metal sulfides	Thioles	Sulfides, Thiophenes	Sulfoxides	Sulfones, R-S(O)O-R
BE /eV	161.9-162.7	163.3-163.7	164.4-164.9	165.7-166.8	168.2-168.7
FWHM /eV	1.0-1.2	1.0-1.2	1.0-1.2	1.0-1.2	1.0-2.0

SI References

1 L. Ni, C. Gallenkamp, S. Paul, M. Kuebler, P. Theis, S. Chabbra, K. Hofmann, E. Bill, A. Schnegg, B. Albert, V. Krewald and I. Kramm Ulrike, *Advanced Energy and Sustainability Research*, 2021, **2**, 2000064.

2 S. Wagner, H. Auerbach, C. E. Tait, I. Martinaiou, S. C. N. Kumar, C. Kübel, I. Sergeev, H.-C. Wille, J. Behrends, J. A. Wolny, V. Schünemann and U. I. Kramm, *Angewandte Chemie International Edition*, 2019, **58**, 10486-10492.

3 R. Taube, *Pure & Applied Chemistry*, 1974, **38**, 427–438.

4 U. I. Kramm, L. Ni and S. Wagner, *Advanced Materials*, 2019, **31**, 1805623.

5 A. Serov, K. Artyushkova and P. Atanassov, *Advanced Energy Materials*, 2014, **4**, 1301735.

6 M. C. Biesinger, B. P. Payne, A. P. Grosvenor, L. W. M. Lau, A. R. Gerson and R. S. C. Smart, *Applied Surface Science*, 2011, **257**, 2717-2730.

7 A. P. Grosvenor, B. A. Kobe, M. C. Biesinger and N. S. McIntyre, *Surface and Interface Analysis*, 2004, **36**, 1564-1574.

8 K. Artyushkova, B. Kiefer, B. Halevi, A. Knop-Gericke, R. Schlogl and P. Atanassov, *Chemical Communications*, 2013, **49**, 2539-2541.

9 F. Jaouen, J. Herranz, M. Lefèvre, J.-P. Dodelet, U. I. Kramm, I. Herrmann, P. Bogdanoff, J. Maruyama, T. Nagaoka, A. Garsuch, J. R. Dahn, T. S. Olson, S. Pylypenko, P. Atanassov and E. A. Ustinov, *Applied Materials and Interfaces*, 2009, **1**, 1623–1639.

10 M. Peuckert, *Surface Science*, 1984, **144**, 451-464.

11 B. J. Lindberg, K. Hamrin, G. Johansson, U. Gelius, A. Fahlman, C. Nordling and K. Siegbahn, *Physica Scripta*, 1970, **1**, 286-298.

12 M. Smith, L. Scudiero, J. Espinal, J.-S. McEwen and M. Garcia-Perez, *Carbon*, 2016, **110**, 155-171.

13 S. Pylypenko, A. Queen, T. S. Olson, A. Dameron, K. O'Neill, K. C. Neyerlin, B. Pivovar, H. N. Dinh, D. S. Ginley, T. Gennett and R. O'Hayre, *The Journal of Physical Chemistry C*, 2011, **115**, 13667-13675.